Electronic properties and quasi-zero-energy states of graphene quantum dots

H. V. Grushevskaya[*] and G. G. Krylov[†]

Physics Department, Belarusian State University, 4 Nezalezhnasti Avenue, 220030 Minsk, Belarus

S. P. Kruchinin ●[‡]

Bogolyubov Institute for Theoretical Physics, NASU, Metrologichna Street 14-b, 03143 Kiev, Ukraine

B. Vlahovic ●

North Carolina Central University, 27707 Durham, North Carolina, USA

Stefano Bellucci ●[§]

INFN-Laboratori Nazionali di Frascati, 54 Via Enrico Fermi, 00044 Frascati, Italy

In this paper, research has been carried out on the electronic properties of nanostructured graphene. We focus our attention on trapped states of the proposed systems such as spherical and toroidal graphene quantum dots (GQDs). Using a continuum model, by solving the Dirac-Weyl equation, and applying periodic boundary conditions of two types, i.e., either with zigzag edges only or with both armchair and zigzag edges, we obtain analytical results for energy levels yielding self-similar energy bands located subsequently one after another on the energy scale. Only for the toroidal quantum dot (owing to the lack of curvature) the distribution of electron density is like Bohr atomic orbitals. However, although the quasi-zero-energy band exists for both spherical and toroidal quantum dots, no electron density is present on this band for the toroidal quantum dot. This causes the formation of a pseudogap between the hole and electron bands because of the absence of the electron density at the quantum dot center, like in the case of an ordinary atom. Conversely, the confinement of the charge-carrier density is observed for both geometries of GQDs.

I. INTRODUCTION

Nanodimensional monolayer graphene patches are promising as a basis for the development of quantum devices. Graphene physics is the physics of massless charge carriers. The nanometer-sized quasicircular graphene monolayer samples, called graphene quantum dots (GQDs), can be chemically synthesized. Chemically synthesized nanoscale GQDs have the form of a quasicircle with a radius in the interval from 3 to 10 nm [1]. By scattering on the physical edges of contacting graphene patches, charge carriers drastically impair their mobility. Moreover, the fact that the Schrödinger equation with a confining parabolic potential satisfactorily describes at least the low-lying states of the synthesized dots means that the distortion of electron-hole physics is possible up to the loss of bipolarity of the material (see e.g., Refs. [2,3] and references therein).

The problem of contacts in graphene electronics can be solved by designing the so-called electrically confined GQDs without physical termination. The electrically confined GQD is a part of the graphene monolayer, separated by a potential barrier from the rest of the monolayer. The electrostatic geometric confinement in a graphene monolayer allows us to finely tune the charge localization and scattering in graphene-based devices. To form an electrically confined GQD, the graphene monolayer deposited on the support is $n(p)$ doped. The local action of an electric field (screening) directed opposite to the electric field of $n(p)$ doping changes locally the type of doping from $n(p)$ to $p(n)$. The resulting n-p or p-n junction is an electrically confined GQD. The $n(p)$ doping of a bulk monolayer can be achieved by applying an electric voltage V_{BG} to the support.

The design of nanoelectronic devices based on graphene n-p (p-n) junctions requires the knowledge of model-independent realistic confining electrostatic potentials. Model-confining potentials for GQDs have been currently offered. However, their shape is determined by the specificity of fabrication method. There are three techniques. First, an electric field of the graphene-doping electrode (back gate) contacting with the support can be locally screened by forming an additional thin (needlelike) metal structure on the surface of the tip of the scanning tunneling microscope (STM) [4,5]. Such quantum dots are called tip-induced ones. Second, under the local action of an electric voltage pulse V_{TG} on the STM tip, the nanometer-sized graphene region is doped with charge carriers of the opposite sign with respect to bulk

[*]grushevskaja@bsu.by
[†]krylov@bsu.by
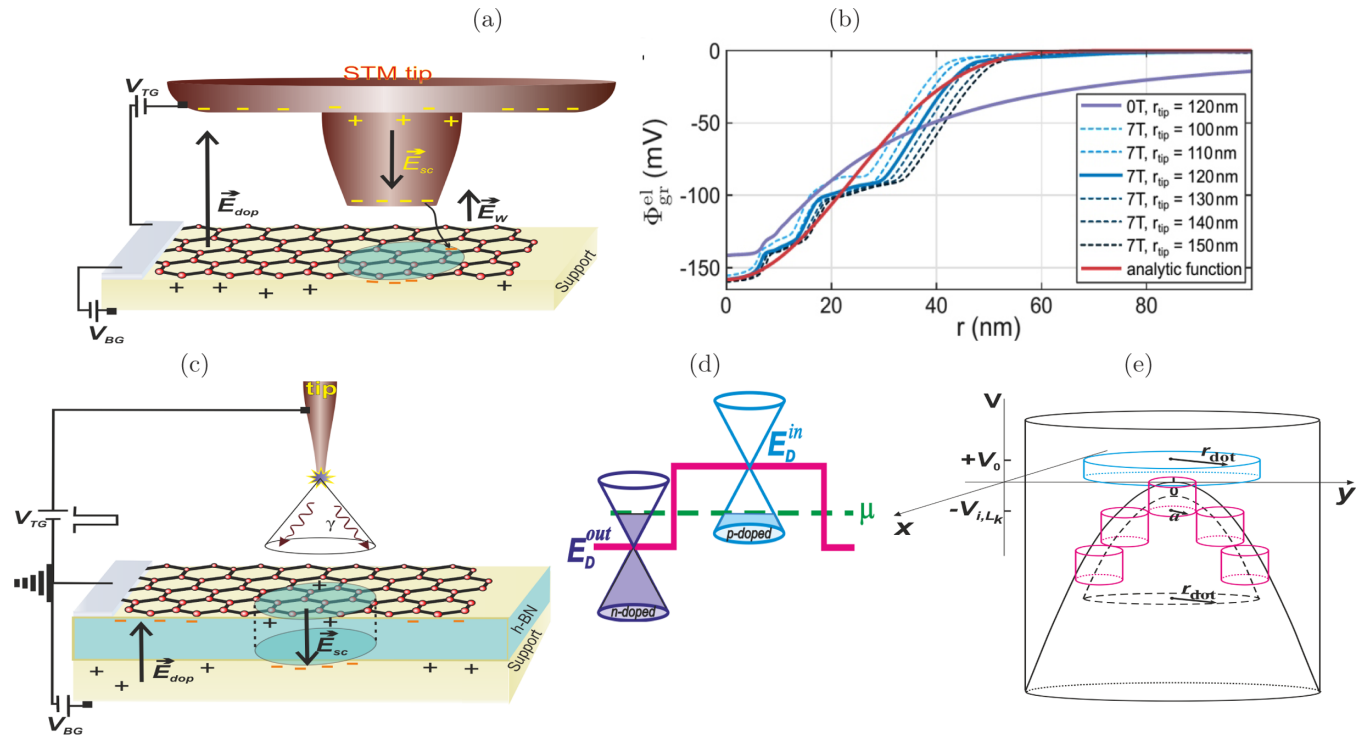[‡]sergeikruchinin@yahoo.com
[§]bellucci@lnf.infn.it

FIG. 1. Sketch of electrical fields creating circular graphene *n-p* and *p-n* junctions and the model potentials confining charge carriers in the junctions. (a) The *n-p* junction is induced by a scanning tunneling microscope (STM) double tip, which consists of a large-radius tip and a small-radius tip attached to the latter at the lowest point. Emerging at application of voltages V_{TG} and V_{BG} to the STM tip (top gate) and support (back gate) an electric field $\vec{E}_{dop}$ dopes the bulk graphene with a positive charge. By polarizing the metallic thin tip, one creates an electric field $\vec{E}_{sc}$, which screens the graphene region located under the tip from the action of $\vec{E}_{dop}$, that locally results in changing *p*-doping to *n*-doping. The level of *n*-doping also depends on the electric field $\vec{E}_W = \Delta \vec{W}/e$ produced by the difference between work functions W_g and W_t of graphene and metal probe tip. (b) Cos-shaped potential reconstructed on experimental data [4]. (c) The *p-n* junction is induced by a pulse of STM-tip voltage. The electromagnetic quanta γ polarize the hexagonal boron-nitride (h-BN) region directly underneath the tip. The electric field $\vec{E}_{sc}$ in this h-BN region, functioning as a negatively charged local embedded gate, positively dopes the graphene region underneath the tip. $\vec{E}_{sc}$ screens the *p*-doped graphene region from an action of the electric field $\vec{E}_{dop}$, which dopes bulk graphene with a negative charge. (d) Schematic of confining-potential measurements over two Dirac band touchings E_D^{in} and E_D^{out} inside and outside the electrostatically confined graphene *p-n* junction, respectively. The Dirac-touching offset produces a radial step potential $V(r)$. The chemical potential μ is marked by a dashed line. (e) Model scattering potentials for the graphene quantum dot (GQD) of radius r_{dot}: a long-wave approximation $V_{i,R_k} \propto -\epsilon_{R_k}(q_i)\Theta(\lambda_i - R)\Theta(a - r)$ of the pseudopotential in Eq. (2.20) (red curves) $R_k = |\vec{R} - \vec{r}|$; a parabolic potential $(-\kappa r^2)$ with a large repulsive potential outside the GQD (black curves); a cylindrical barrier potential $V = +V_0\Theta(r_{dot} - R) \geqslant 0$, $V_0 > 0$ (blue curves). The +, − signs indicate the charge polarities in the tip and in graphene with support.

graphene [6]. A mechanism for creating a local *p(n)*-doped region by the second method is the ionization of defects in the hexagonal boron-nitride (h-BN) layer of support by an electric-field pulse; the released (migrated) charges screen the electric field acting from the side of the support, that is, equivalent to local *p(n)*-doping. In this case, the support plays a role of a back gate, and the local *p(n)*-doping is equivalent to the fabrication of a local embedded gate. Third, the shielding embedded gate can be effectively formed as the part of metal support, which remains defect free during the epitaxial growth of the graphene on its surface [7]. The advantage of the field doping used in the first two methods is the absence of a Fermi level shift under the action of the chemical potential.

The confining potential of the tip-induced GQD is subjected to the strong influence of electric fields due to peculiarities of the field spatial configuration, schematically presented in Fig. 1(a). Since the screened region is bound to the STM double tip and, correspondingly, the tip-induced

GQD is bound functionally to the tip, while the structure of such junctions was not observed in the images. The atomlike nature of these graphene *p-n* junctions is revealed in the experimental dependence of a derivative of the tunneling current dI/dV on voltages V_{TG} and V_{BG}. The dependence is like the local density of states (LDOS) for a tight-binding Hamiltonian of graphene charge carriers moving in a potential of the Thomas-Fermi atom model [5]. According to this estimate, the quantum dot is an artificial atom with a huge number of electrons, as the effective electric charge of Coulomb potential or the Coulomb coupling $\beta = (Z/\epsilon_G)\alpha c/v_F$, which confines charge carriers in the tip-induced junction, takes on values typical for a supercritical regime of ultraheavy atoms. Here, Z is a local unscreened charge, c is the speed of light, v_F is the Fermi velocity, and ϵ_G is the effective dielectric constant of bulk graphene $\epsilon_G \approx 5$ [8]. The atomlike distribution of the electron (hole) density in such quantum dots is fitted by a continuous Thomas-Fermi-like approximation for a potential $U(r)$ confining electrons (holes):

$U(r) = \mathrm{sgn}(n)\hbar v_F \sqrt{\pi |n(r)|}$. Here, $n(r)$ is a charge density (for holes in p-n junctions or for electrons in n-p junctions). The confining model potential based on the Thomas-Fermi model is a two-step potential [5], and *ab initio* full tight-binding calculations with a Poisson's equation predict a staircase form for the confining potentials [see Fig. 1(b)] [4,9,10].

Since the back gate and the created embedded gate exist independently of the STM tip, the atomlike structure of GQDs fabricated by the second and thid methods can be imaged by a STM probing of their LDOS using voltages that practically do not change the initial configuration of the gate electric fields shown schematically in Fig. 1(c). The imaging allows us to construct the confining electrostatic potential directly from the experimental values of the touchings $E_D^{(i)}, i = 1, 2, \ldots$ between the Dirac graphene valence and conduction bands. For example, a radial step potential is constructed based on the two values of E_D inside and outside the small-radius quantum dot [see Fig. 1(d)]. A parabolic potential as an infinite set of single-step radial potentials is used to describe large GQDs [see Fig. 1(e)]. When constructing a model confining potential for the third fabricating method, it is also necessary to anticipate an offset of the chemical potential μ for GQD after doping of graphene with metal atoms.

A feature of the scattering Dirac fermions with mass m is the existence of delocalized modes among scattered ones under the condition $V > 2m$ imposed on the potential barrier V [11]. The delocalized modes are called transmission resonances, and the tunneling process is called the Klein one (see also Ref. [12] and references therein). The fermions pass freely through the potential barrier at normal incidence on the boundary of the barrier V for phases that are multiples of $\pi \pm 2\pi n$; $n = 0, 1, \ldots$ [13]. For the massless graphene fermions, the transmission resonances will always be present among the scattered modes. Assuming that the effects of Klein tunneling will always distort the electrostatic confinement of massless charge carriers, the variety of solutions to the problem of pseudo-Dirac fermions in electrostatically confined graphene p-n(n-p) junctions can be narrowed down to the subvariety of levels localized near the Fermi level (quasi-zero-energy levels or whispering gallery modes). Due to the orbital motion of charge carriers, the production of electron-hole pairs does not occur. Unfortunately, for the massless fermions, a condition selecting eigenstates, which are localized at the edge of the radial step barrier and behave like to Dirac δ function, gives a single level or has unphysical solutions, depending on the GQD parameters [14,15]. In Ref. [7], the set of states with one real eigenvalue is speculatively expanded by adding solutions with complex eigenvalues, manipulating (juggling) with them to achieve an apparent similarity between the calculated LDOS and dI/dV. The nonrelativistic tight-binding Hamiltonians, which fundamentally do not possess Klein scattered modes, narrow the possible types of edge spatial configurations at which there is a zero-energy level in the quasicircular GQD [16]. It turns out that the spectra of zigzag-edged quasicircular GQDs (zigzag edges at the boundary prevail) and zigzag-edged hexagonal GQDs host only one zero-energy level, and the tight-binding GQD model of arbitrary shape does not predict the modes localized at the boundary of the cavity [17–20]. A simplified continuous pseudo-Dirac

Hamiltonian with a radial step potential hosts a zero eigenvalue at the zigzag-boundary condition. However, among the eigenvalues of the Hamiltonian, there are no zero or quasi-zero energies at the so-called infinite-mass boundary condition, meaning that the region outside the dot is forbidden, or the type of all edges is an armchair one, and correspondingly, the boundary is nonmetallic [18,21,22]. Another mechanism for the emergence of the zero-energy level is associated with the exciton instability in graphene [23]. It can be assumed that electron-hole pairs become Keldysh-type exciton states, energetically favorable in a low-dimensional system with the dielectric constant ϵ (in this case, in one dimension). The screened electron-hole interactions added to the continuous pseudo-Dirac fermion model with a radial step potential at the infinite-mass boundary condition result in a zero-energy level [24]. Unfortunately, even when using the low dielectric constant $\epsilon_G = 2.5$ (while experiments give $\epsilon_G = 5$), the exciton binding energy is very small, i.e., at least two times less ($\sim$50 meV) than the probing voltage (electrostatic potential) 0.1–1 eV. Therefore, the exciton polarization cannot be the mechanism responsible for the existence of zero-energy states.

Thus, the problem of an existing zero-energy level for a graphene junction with arbitrary-edged configurations is still unsolved. Moreover, the stability of the experimentally observed quasi-zero-energy levels can be not only and not that much related to the peculiarities of the Klein tunneling process. There are experimental indications that long-lived scattered resonances can be at deep enough levels of confining staircase potentials [5]. Also, large p-n (n-p) junctions fabricated by the second technique are characterized by a huge number of quasistationary levels far from the GQD edge. This could be an indication that the GQDs can exist for quite a long time in states other than quasi-zero-energy modes. The confinement of massless fermions in the multistep potential can be considered simplistically as the confinement of a pseudo-Dirac fermion in a parabolic potential. Unfortunately, since the quasi-zero-energy levels at the edge of such a GQD are spurious ones, the assignment of the levels in the parabolic confining potential to the long-lived Klein resonances cannot be considered as correctly justified [8].

Generally speaking, since GQDs are many-body artificial atoms, their models must have a lot of quasi-zero-energy modes. The phase condition for the existence of transmission resonances has nothing in common with their spatial configuration and can expand the search for the solutions to the region of Klein transmission modes delocalized in a limited GQD region. In addition, the experimental LDOS of electrostatically confined junctions is polarized [6]. Until now, no models of such exotic states have been proposed. The amazing fact that the modern GQD models cannot have quasi-zero-energy levels, except for the actual zero-energy level, should be interpreted as a huge problem. Without a solution to such a problem, there can be no talk of the physics of GQDs.

Therefore, the search for the selection criteria of GQDs with quasi-zero-energy levels and transmission resonances, delocalized in a limited spatial area, is a difficult and unsolved problem. The lack of models, in which a quasi-zero-energy band emerges, prevents the development of methods to tune up the graphene junction in such a way that its modes
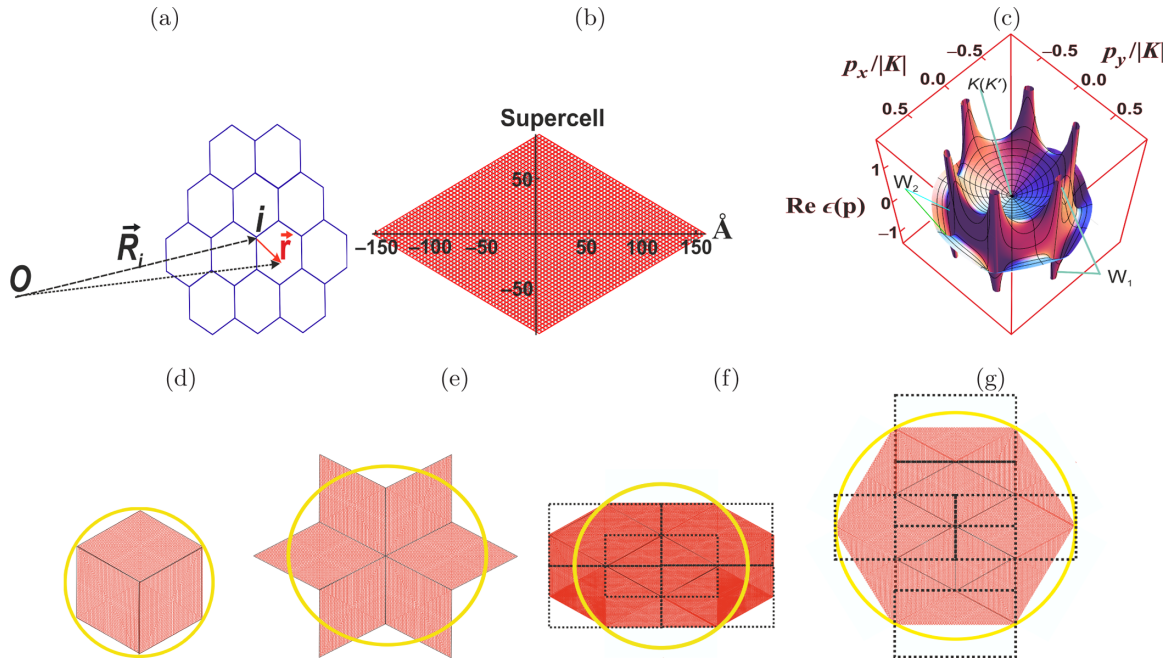
FIG. 2. Scheme of a graphene quantum dot (GQD): (a) the ith atom C is located at the ith site with radius vector $\vec{R}_i$, and $\vec{r}$ is a radius vector of the p_z electron relative to the ith lattice site, O is a reference point. (b) The GQD supercell used to calculate a quantum dot with torus topology includes 51×51 primitive cells (100×150 Å). Splitting of Dirac cone into replicas for graphene in the Dirac-Hartree-Fock quasirelativistic approximation q^4 for the exchange interactions. Two W_1, W_2 of the six pairs of Weyl nodes-antinodes: (c) two sources and two sinks and the Dirac valley $K(K')$ are indicated. In (d) and (e), we describe model quantum dots produced by three and six rhombic unit supercells, respectively. Edges of these quantum dots are zigzag ones. In (f) and (g), we depict model quantum dots produced by four and eight rectangular unit supercells, respectively. The quantum dot in figure (f) holds zigzag as well as armchair edges. The edges of the quantum dot in figure (g) are in the armchair configuration. Radius of the yellow-colored circumference in figures (d)–(g) can be interpreted as a radius of the quasicircular quantum dot. Rectangular unit cells are labeled by dotted lines.

do not turn out to be short-lived resonances, and Klein transmission resonances are delocalized in a limited area of space. Therefore, realization of devices based on the tailored charge confinement in a graphene monolayer is still challenging.

In this paper, we simulate electrostatically confined GQDs, using a quasirelativistic tight-binding Hamiltonian of massless fermions in monolayer graphene. We present a discrete model of the GQD and its continuous limit to describe realistic electrostatically confined GQDs. To do this, we use a high-energy $\vec{k} \cdot \vec{p}$ massless-fermions Hamiltonian. A band structure obtained from the Hamiltonian holds the Dirac touching and six Weyl node-antinode pairs as minibands near the valley $K(K')$ of the graphene Brillouin zone. Then we look for a pseudopotential barrier given by a set of well potentials for distinct carbon atoms of the GQD. We discover two topologically different scenarios of the confinement in a quantum dot.

II. MODEL OF AN ELECTRICALLY CONFINED GQD AND THEORY

A graphene monolayer quantum dot consisting of carbon atoms is shown schematically in Fig. 2(a). Let a model quantum dot be considered as a "large atom." Its core ith electrons, by definition, are p_z electrons of jth C atoms, $j \neq i$. The kth p_z electron of the kth C atom plays the role of an external valence electron. Let the kth C atom be placed at the lattice site with a radius vector $\vec{R}_k$. The radius vector $\vec{r}$ will be

calculated with respect to the nearest lattice site and is a radius vector of the electron in the atom. The radius vector $\vec{X}_k$ of the valence electron of the kth atom is given by the expression

$$\vec{X}_k = \vec{R}_k + \vec{r}. \tag{2.1}$$

A model GQD has been constructed in the following way. The graphene primitive cell has basic vectors $\vec{b}_1 = a(3/2, \sqrt{3}/2)$, $\vec{b}_2 = a(3/2, -\sqrt{3}/2)$, and two atoms (A and B) in the cell. Here, a is the length of the sp^2-hybridized C-C bond. We construct a rhombic region consisting of $(2n_1 + 1)(2n_2 + 1)$ primitive cells of graphene for $n_1 = 25$, $n_2 = 25$, which is shown in Fig. 2(b).

A. Folding zone approximation

The energy levels of a GQD can be approximately found by the "folding zone" method in the same way as for single-walled carbon nanotubes (CNTs). Electronic states of CNTs are restricted to wave vectors that fulfill the quantization condition [25]

$$\vec{k}_\perp \cdot \vec{C} = 2\pi m, \quad m = -\frac{N}{2} + 1, \ldots, \frac{N}{2}, \tag{2.2}$$

where $\vec{k}_\perp$ is a wave vector in the direction perpendicular to the CNT axis, $\vec{C}$ is a chiral vector of the CNT, N is the number of graphene hexagonal unit cells within a CNT unit cell, and m is an index of a one-dimensional (1D) band. The condition in Eq. (2.2) is the so-called "Born–von Karman" condition.

Contrary to the CNT case, the wave vector $\vec{k} = (k_x, k_y)$ of a charge carrier in the dot is quantized in two directions. Moreover, the quantum dots can be constructed with topologies: sphere S^2 and torus $S^1 \times S^1$ in the following way. The dot topologically equivalent to the sphere is formed by rhombuses inscribed into rectangular supercells. Such a geometrical structure can be obtained by a shift on a half-period of the rectangular lattice. The sphere topology is obtained by identifying all vertices of the rhombus and gluing adjusting its sides. In the case of the rectangular unit cell, a quantum dot can be produced, for example, by four or eight supercells. The quantum dots of this type are presented in Figs. 2(f) and 2(g). All edges of the eight-supercell dot are in armchair configurations. The edges of the four-supercell dot are both in armchair and zigzag configurations. Since the symmetry group for the superlattice with the rectangular unit cell is a nonsymmorphic one, there are no punctured points.

Since the basis vectors of the rectangular unit are $\vec{C}_1 = (2n_1 + 1)\vec{b}_1 + (2n_2 + 1)\vec{b}_2$ and $\vec{C}_2 = (2n_1 + 1)\vec{b}_1 - (2n_2 + 1)\vec{b}_2$, the quantization conditions for the S^2-type GQD read

$$[(2n_1 + 1)\vec{b}_1 + (2n_2 + 1)\vec{b}_2] \cdot \vec{k} = 2\pi m_1,$$
$$m_1 = -\frac{N_{\text{dot}}}{2} + 1, \ldots, \frac{N_{\text{dot}}}{2};$$
$$[(2n_1 + 1)\vec{b}_1 - (2n_2 + 1)\vec{b}_2] \cdot \vec{k} = 2\pi m_2,$$
$$m_2 = -\frac{N_{\text{dot}}}{2} + 1, \ldots, \frac{N_{\text{dot}}}{2}. \tag{2.3}$$

Here, $N_{\text{dot}} = (2n_1 + 1)(2n_2 + 1)$ is the total number of graphene hexagonal unit cells within the supercell. For the model quantum dot shown in Fig. 2(b), the number of levels $(N_{\text{dot}} + 1)^2 \approx 6.7 \times 10^6$.

In the case of the rhombic unit cell, a quantum dot can be generated by, for example, three or six supercells with one common vertex. Since the vertex is the punctured point of the circle, the topology of these dots is a toroidal one. The quantum dots of this type have zigzag edges only and are presented in Figs. 2(d) and 2(e). The torus is obtained by identifying of the opposite sides of the rhombic supercell (at first by gluing with twisting into a cylinder, then by gluing the latter into a torus).

The basis vectors of the rhombic supercell are $\vec{C}_1 = (2n_1 + 1)\vec{b}_1$, $\vec{C}_2 = (2n_2 + 1)\vec{b}_2$. Therefore, quantized wave vectors for the toroidal-type dot are determined as

$$(2n_1 + 1)\vec{b}_1 \cdot \vec{k} = 2\pi m_1, \quad m_1 = -\frac{N_{\text{dot}}}{2} + 1, \ldots, \frac{N_{\text{dot}}}{2};$$
$$(2n_2 + 1)\vec{b}_2 \cdot \vec{k} = 2\pi m_2, \quad m_2 = -\frac{N_{\text{dot}}}{2} + 1, \ldots, \frac{N_{\text{dot}}}{2}. \tag{2.4}$$

The pair of numbers (m_1, m_2) entering the formulas in Eqs. (2.3) and (2.4) is a multi-index of a superlattice band. Inverse-superlattice wave vectors $\vec{G} = n_1\vec{G}_1 + n_2\vec{G}_2$ lie inside the single-layer graphene Brillouin zone. Here, $\bar{G}_1, \bar{G}_2$ are basic vectors of the inverse-superlattice, and n_1, n_2 are integers. The superlattice Brillouin zone is very small, and accordingly, quasiparticle momenta $\vec{p}_s$, $(n_1\vec{C}_1 + n_2\vec{C}_2) \cdot \vec{p}_s = 2\pi L$, which

are due to the translational symmetry of the problem, are small also. Here, L is an integer. Therefore, we can neglect $\vec{p}_s$, assuming that the bands are degenerated over $\vec{p}_s$ (a dependence on wave number p_s is absent). These zero-dimensional (0D) bands is what we name energy levels of our quantum dot model. The first advantage of the proposed "momentum" boundary conditions in Eqs. (2.3) and (2.4) is in a small number of variants (only two). The nodes of the wave function on the boundary signify that the source of the wave and, correspondingly, an outward current, are absent. The second advantage is that the radius of a quantum dot with a given topology determines uniquely a supercell combination forming the dot and, accordingly, the zigzag and armchair edge configuration of its boundary.

Thus, we assume that the STM experiment probes the many-electron structure formed under the action of an electric field in a region consisting of supercells. Valence electrons of the structure move in an electric field of core electrons. The latter will be described within a pseudopotential method. The pseudopotential corrections are considerably larger than contribution of momenta $\vec{p}_s$.

Further, using a folding zone approach, we will calculate pseudopotential-bending 0D bands of single-layer graphene in a superlattice potential. In addition, the topology of toroidal or spherical types is a sign of the charge density distribution on circular orbits. The above makes it possible to assign simulated quantum dots to a quasicircular type. The latter will also be confirmed by the simulation results.

We use a monolayer graphene model $\vec{k} \cdot \vec{p}$ Hamiltonian $\hat{H}_D$ to determine the energy levels $\epsilon(q_{m_1, m_2})$ of the GQD in the folding zone approximation. Meanwhile, one has to work with the whole Brillouin zone rather than the first one. Let a wave vector $\vec{k}_{m_1, m_2}$, satisfying either the quantization conditions in Eq. (2.3) or Eq. (2.4), be associated with the reduced wave vector $\vec{q}_{m_1, m_2}$ as the difference between $\vec{k}_{m_1, m_2}$ and the nearest Dirac point (valley) $K(K')$ of the Brillouin zone. The Hamiltonian $\hat{H}_D$ is obtained within the quasirelativistic Dirac-Hartree-Fock self-consistent field approach (see Refs. [26,27]). It is a high-energy $\vec{k} \cdot \vec{p}$ Hamiltonian in a q^4 approximation for the quasirelativistic quantum exchange. The approximation is the series expanded around the Dirac point $\vec{K}(\vec{K}')$ in powers of difference $\vec{q} = \vec{p} - \vec{K}$ between the quasiparticle momentum $\vec{p}$ and $\vec{K}(\vec{K}')$. The expansion on $q \equiv |\vec{q}|$ is produced up to the terms of $O(q^4)$ inclusively. The deviations of eigenvalues of $\hat{H}_D$ from the low-energy massless pseudo-Dirac fermion model are of the order of $|q|^4$. Contrary to the nonrelativistic graphene model, energy levels of the quasirelativistic graphene model are Kramer's doublets. The Kramer's doublet represents itself two levels at which electrons are placed with the opposite signs of spin, and in the absence of quantum exchange, the levels are degenerated. The relativistic quantum exchange removes degeneration on spin outside the Dirac valley, violating the particle-hole symmetry so that the degeneration of the Dirac point is lifted outside the Dirac valley, and six minibands emerge near the Dirac point. Due to the removal of the degeneracy of the Kramer's doublets, each miniband represents a Weyl node-antinode pair. Figure 2(c) demonstrates the band structure of the graphene model characterized by the Dirac touching in the point $K(K')$

and six Weyl node-antinode pairs. Let us note that, as opposed to our quasirelativistic high-energy graphene model, for the low-energy $\vec{k} \cdot \vec{p}$ Hamiltonian of massless pseudo-Dirac fermion, a Weyl node-antinode pair appears after removing of Dirac point degeneration over the pseudospin in a three-dimensional topological insulator so that a Fermi arc along axis Z is observed (see, for example, Ref. [28]).

The folding zone approximations of quantum-dot wave functions resemble (look similar) to harmonic (sinusoidal) discrete solutions (standing waves) of a quantum mechanical problem on a particle in a 1D rectangular well with infinitely high walls. The wave functions are the bispinors $\psi^T = (\psi_\uparrow, \psi_\downarrow) = \exp\{-i\vec{q}_{m_1,m_2} \cdot (\vec{r} + \vec{R}_k)\}(u_\uparrow, u_\downarrow)$ of charge carriers with the energies $\epsilon(q_{m_1,m_2})$. Here, $\uparrow$ and $\downarrow$ designate spinor components with spin up and down, respectively. Here, T is the transposition operation, $u_{\uparrow(\downarrow)}$ are periodic functions: $u_{\uparrow(\downarrow)}(\vec{r} + \vec{R}_k) = u_{\uparrow(\downarrow)}(\vec{r} + \vec{R}_k + \vec{a}_S)$, and $\vec{a}_S$ is a supercell vector.

We sort the energy levels $\epsilon(q_{m_1,m_2})$, in the energy increase order, by introducing an index i for the energies and wave vectors and introduce a formal index R_k according to the above-presented form of wave function. Therefore, in what follows, we will denote the energies by $\epsilon_{R_k}(q_i)$. We emphasize that the energy does not depend upon R_k.

Thus, the following set of eigenenergies $\pm\epsilon_{R_k}(q_i)$ and eigenstates $\psi_i^{(0)}(\mp q_i, \vec{r} + \vec{R}_k) = \exp[\mp\iota\vec{q}_i \cdot (\vec{r} + \vec{R}_k)]u(\vec{r} + \vec{R}_k)$, $u = (u_\uparrow, u_\downarrow)^T$ for the GQD in the folding zone approximation is

$$\left\{\pm\epsilon_{R_k}(q_i), \ \psi_i^{(0)}(\mp\vec{q}_i, \vec{r} + \vec{R}_k)\right\}_{i,k=1,\ldots,N_{\text{dot}}}, \quad (2.5)$$

where the upper sign $+$ is related to electrons, and the lower sign $-$ corresponds to holes.

In the following section, we construct a pseudopotential in which charge carriers of GQDs move.

B. Continuous GQD model with pseudopotential

In a graphene monolayer, all p_z electrons form pairwise molecular π orbitals. Here, π electrons located inside and outside of the edges of a monolayer patch turn out to be unpaired among π electrons, composing an artificial atom of the type of a GQD. These electrons occupy orbitals of the GQD singly and are valence electrons of the artificial atom.

If not all electrons of the many-electron system (in our case, this is the artificial atom) are coupled, a Hamiltonian of the system includes nonpaired-electron potentials that polarize an atomic core (an exchange hole exists). The simplest one-body method of approximate account of the atom polarization in the electric field of the valence electron is based on the Phillips-Kleinman cancellation theorem, which states that all electrons, except an external orbital, are coupled, and the valence electron moves in a pseudopotential which is added to the atomic core potential [29].

Therefore, one has to add a pseudopotential operator to the high-energy $\vec{k} \cdot \vec{p}$ Hamiltonian $\hat{H}_D$ [30,31]. Let $|\Psi\rangle$ be a vector of bispinor state in a Hilbert space $\mathcal{H}$ with coordinates $\langle \vec{X}_1, \sigma_1; \ldots; \vec{X}_{N_{\text{dot}}}, \sigma_{N_{\text{dot}}}|\Psi\rangle$, written in ordinary space representation through the radius vectors of charge carriers in the monolayer

$$|\Psi\rangle = \sum_{n_1,\ldots,n_m=1}^{N_{\text{dot}}} \sum_{\sigma_{n_1},\ldots,\sigma_{n_m}} \int d\vec{X}_{n_1}\ldots d\vec{X}_{n_m}|\vec{X}_{n_1}, \sigma_{n_1}; \ldots; \vec{X}_{n_m}, \sigma_{n_m}\rangle\langle \vec{X}_{n_1}, \sigma_{n_1}; \ldots; \vec{X}_{n_m}, \sigma_{n_m}|\Psi\rangle. \quad (2.6)$$

Here, σ_i is a spin of the ith electron. In this Dirac bracket representation of wave functions for the Fock space [32], the coordinates (wave functions) $\langle \vec{X}_{i_m}, \sigma_{i_m}|\Psi\rangle \equiv [\psi_{m,\uparrow}(\vec{X}_i), \psi_{m,\downarrow}(\vec{X}_i)]^T = \psi_m(\vec{X}_i)$ of mth particle states $|\psi_m\rangle$ in Eq. (2.6) are obtained by an action of the projectors $|\vec{X}_i, \sigma_i\rangle\langle \vec{X}_i, \sigma_i|$, satisfying the resolution of identity $\hat{I} = \sum_{\sigma_i} \int d\vec{X}_i|\vec{X}_i, \sigma_i\rangle\langle \vec{X}_i, \sigma_i|$. Here, $|\vec{X}_i, \sigma_i\rangle$ and $\langle \vec{X}_i, \sigma_i|$ are a vector of the Hilbert space $\mathcal{H}$ and a vector conjugated to it.

The one-body Hamiltonian operator for an electron moving in the quantum dot pseudopotential reads

$$\hat{H}_D|\psi_m\rangle = \left(\epsilon_m - \sum_{j=1}^{N_{\text{dot}}} \hat{\epsilon}^\dagger P_j\right)|\psi_m\rangle, \quad (2.7)$$

where the second term on the right-hand side of Eq. (2.7) is the pseudopotential operator $\sum_{j=1}^{N_{\text{dot}}} \hat{\epsilon}^\dagger P_j$ determined through a hole energy operator $\hat{\epsilon}^\dagger$ and a projection operator

$$P_j = \int d\vec{X}_k d\vec{X}_i|x_k\rangle\langle x_k|\psi_j\rangle\langle \psi_j|x_i\rangle\langle x_i|, \quad (2.8)$$

coefficient matrices $\langle x_k'|P_j|x_i'\rangle$ of which have the following form $\langle x_k'|P_j|x_i'\rangle = \begin{bmatrix} \psi_{j\uparrow}(\vec{X}_k')\psi_{j\uparrow}^*(\vec{X}_i') & \psi_{j\downarrow}(\vec{X}_k')\psi_{j\uparrow}^*(\vec{X}_i') \\ \psi_{j\uparrow}(\vec{X}_k')\psi_{j\downarrow}^*(\vec{X}_i') & \psi_{j\downarrow}(\vec{X}_k')\psi_{j\downarrow}^*(\vec{X}_i') \end{bmatrix}$; ϵ_m is a mth eigenvalue of $\hat{H}_D$.

We use a representation where the operator $\hat{\epsilon}^\dagger$ is a matrix, which elements $\{\epsilon_{kc_i}\} \equiv \{\epsilon_{R_k-R_i}(q_{c_i})\}$ belong to the set in Eq. (2.5). Here, on the definition of valence electron, $\epsilon_{kc_i} = 0$ at $k = c_i$. In this representation, Eq. (2.7) is an equation of motion for the valence kth electron with a radius vector $\vec{X}_k = \vec{r} + \vec{R}_k$:

$$\hat{H}_D\psi_k(\vec{r} + \vec{R}_k) + \sum_{i,c_i\neq k}^{N_{\text{dot}}-1} \epsilon_{kc_i}P_{c_i}\psi_{c_i}(\vec{r} + \vec{R}_k)$$

$$= E_k\psi_k(\vec{r} + \vec{R}_k), \quad k = 1, \ldots, N_{\text{dot}}. \quad (2.9)$$

Here, $P_{c_i} = \int d\vec{X}_n\psi_k(\vec{X}_n)\psi_{c_i}^*(\vec{X}_n)$, $\epsilon_{kc_i}\psi_{c_i}(\vec{X}_k) \equiv \hat{\epsilon}^\dagger\psi_{c_i}(\vec{X}_k)$: $\epsilon_{kc_i}\psi_{c_i}(\vec{X}_k) = \int d\vec{X}_{c_i}\langle x_k|\hat{\epsilon}^\dagger|x_{c_i}\rangle\langle x_{c_i}|.\psi_{c_i}\rangle$.

Since a quantum dot consists of sufficiently many atoms, one can construct its continuous model in a hydrodynamic limit $|\vec{R}_{k+1} - \vec{R}_k| = a \to 0$, $r \to 0$. A radius vector $\vec{R}$ of a point in the continuous GQD model takes the values of radius

vectors of lattice sites

$$\vec{R} = \vec{R}_1, \vec{R}_2, \ldots, \vec{R}_{N_{\text{dot}}}. \tag{2.10}$$

A derivative $\frac{\partial}{\partial \vec{R}}$ for the continuous GQD model is determined in the following way:

$$\frac{\partial}{\partial \vec{R}} \Psi(\vec{R}) \stackrel{\text{def}}{=\!=} \left\{ \frac{\psi_k(\vec{R}_{k+1}) - \psi_k(\vec{R}_k)}{\vec{R}_{k+1} - \vec{R}_k} \right\} \Big|_{k=1}^{N_{\text{dot}}}$$

$$= \left\{ \frac{\psi_k(\vec{R}_k + \vec{a}) - \psi_k(\vec{R}_k)}{\vec{a}} \right\} \Big|_{k=1, \, a \to 0}^{N_{\text{dot}}}, \tag{2.11}$$

where $\Psi(\vec{R})$ is a GQD wave function defined by the following expression:

$$\Psi(\vec{R}) \in \{\psi_k(\vec{r} + \vec{R}_k)\}|_{k=1, r=a}^{N_{\text{dot}}}. \tag{2.12}$$

Using the definition in Eq. (2.11), one can determine a convolution $\vec{\sigma} \cdot \frac{\partial}{\partial \vec{R}} \Psi_{v\uparrow(\downarrow)}$ between the derivative of up (down)-spinor component $\Psi_{v\uparrow(\downarrow)}$ and the 2D vector of the Pauli matrices $\vec{\sigma} = (\sigma_x, \sigma_y)$ for a vth electron as

$$\vec{\sigma} \cdot \frac{\partial}{\partial \vec{R}} \Psi_{v\uparrow(\downarrow)}(\vec{R})$$

$$= \sum_{i=1}^{2} \sigma_i \frac{\partial}{\partial x_i} \Psi_{v\uparrow(\downarrow)}$$

$$= \sum_{i=1}^{2} \sigma_i \left\{ \frac{\psi_{v\uparrow(\downarrow)}[\vec{R}_k + (\vec{e}_i, \vec{a})\vec{e}_i] - \psi_{v\uparrow(\downarrow)}(\vec{R}_k)}{(\vec{e}_i, \vec{a})} \right\} \Big|_{k=1, \, a \to 0}^{N_{\text{dot}}}$$

$$\equiv \vec{\sigma} \cdot \vec{\nabla}_{\vec{R}} \Psi_{v\uparrow(\downarrow)}(\vec{R}), \tag{2.13}$$

where $\vec{e}_i, \ i = 1, \ 2$ are orthonormal vectors along the coordinate axes X, Y; $(\cdot, \cdot)$ is a scalar product, $\vec{R}_i = x_i \vec{e}_i$. Then considering E_k is obtained by the action of the operator $i\hbar \frac{\partial}{\partial t}$ on $\psi_k(\vec{r} + \vec{R}_k)$: $E_k \psi_k(\vec{r} + \vec{R}_k) = i\hbar \frac{\partial}{\partial t} \psi_k(\vec{r} + \vec{R}_k)$, the system of equations in Eq. (2.9) in the hydrodynamic limit can be rewritten as

$$\left\{ \hat{H}_D \psi_k(\vec{r} + \vec{R}_k) + \sum_{c \neq k} \epsilon_{kc} P_c \psi_c(\vec{r} + \vec{R}_k) = E \psi_k(\vec{r} + \vec{R}_k) \right\}_{k=1, r \to a}^{N_{\text{dot}}}. \tag{2.14}$$

Using the definitions in Eqs. (2.10)–(2.12) and the definition of the projection operator, one gets an equation of motion for the valence vth electron in a pseudopotential V_{GQD}:

$$\hat{H}_D |\Psi_v\rangle + \sum_{i=1, c_i \neq v}^{N_{\text{dot}}-1} |\Psi_{c_i}\rangle \epsilon_{c_i}(\vec{R}) \langle \Psi_{c_i} | \Psi_v \rangle = E |\Psi_v\rangle. \tag{2.15}$$

Here, $V_{\text{GQD}} \equiv \sum_{i=1, c_i \neq v}^{N_{\text{dot}}-1} |\Psi_{c_i}\rangle \epsilon_{c_i}(\vec{R}) \langle \Psi_{c_i}|$, a matrix $\epsilon_{c_i}(\vec{R})$ is determined by the expression $\epsilon_{c_i}(\vec{R}) \in \{\pm \epsilon_{R_k - R_i}(q_{c_i})\}_{k=1,\ldots,N_{\text{dot}}}$ entering the expression in Eq. (2.5). A scalar product $\langle \Psi_{c_i} | \Psi_v \rangle = \sum_{\sigma} \int \langle \Psi_{c_i} | \vec{R}', \sigma \rangle \langle \vec{R}', \sigma | \Psi_v \rangle \, d\vec{R}'$ of the wave functions $|\Psi_{c_i}\rangle$ and $|\Psi_v\rangle$ of the core and valence electrons of the GQD and, consequently, the operator V_{GQD} are constructed on a basic set of the functions entering the expression in Eq. (2.5):

$$\langle \Psi_{c_i} | \Psi_v \rangle = \sum_{k=1}^{N_{\text{dot}}} \psi_{R_k}^{(0)\dagger}(\mp \vec{q}_{c_i}, \vec{R}_k) \psi_{R_k}^{(0)}(\mp \vec{q}_v, \vec{R}_k), \tag{2.16}$$

and

$$\langle \Psi_{c_n} | V_{\text{GQD}}(\vec{R}) | \Psi_{c_m} \rangle$$

$$= \sum_{i=1, c_i \neq v}^{N_{\text{dot}}-1} \langle \Psi_{c_n} | \Psi_{c_i} \rangle \epsilon_{c_i}(\vec{R}) \langle \Psi_{c_i} | \Psi_{c_m} \rangle$$

$$= \sum_{i=1, c_i \neq v}^{N_{\text{dot}}-1} \sum_{k,l=1}^{N_{\text{dot}}} \psi_{R_k}^{(0)\dagger}(\mp \vec{q}_n, \vec{R}_k) \psi_{R_k}^{(0)}(\mp \vec{q}_{c_i}, \vec{R}_k)$$

$$\times \epsilon_{R_k - R_l}(q_{c_i}) \psi_{R_l}^{(0)\dagger}(\mp \vec{q}_{c_i}, \vec{R}_l)$$

$$\times \psi_{R_l}^{(0)}(\mp \vec{q}_{c_m}, \vec{R}_l). \tag{2.17}$$

To reveal distinctive features from known potentials, let us find an approximation of the pseudopotential in Eq. (2.17) schematically in the δ vicinity of the Dirac point, $\delta \ll 1$: $q_{c_n}, q_{c_m}, q_{c_i} \to 0$. To do it, we substitute Eq. (2.5) into Eq. (2.17), assuming $q_{c_n} \to q_{c_m}$ at $r = a$:

$$V_{n, \vec{R}_s}(\vec{r}) = \lim_{q_{c_n} \to q_{c_m}} \pm \sum_{\sigma, \sigma'} \sum_{i=1, c_i \neq v}^{N_{\text{dot}}-1} \sum_{k,l=1}^{N_{\text{dot}}} |u|_\sigma^2(\vec{r} + \vec{R}_k)$$

$$\times |u|_{\sigma'}^2(\vec{r} + \vec{R}_l) \exp[\pm i(\vec{q}_{c_n} - \vec{q}_{c_i}) \cdot (\vec{R}_k - \vec{R}_l)]$$

$$\times \epsilon_{R_s}(q_i) \Theta(r - a), \quad i \neq k. \tag{2.18}$$

Here, $\vec{R}_s = \vec{R}_k - \vec{R}_l$, $\Theta(r - a)$ is a Heaviside Θ function. Changing summation on i, k, l, by integration in the expression in Eq. (2.18) and using the periodicity property of states $u_{\uparrow(\downarrow)}$, we find the pseudopotential in the long-wave approximation:

$$V_{n, \vec{R}_s}(\vec{r}) = \pm \sum_{\sigma, \sigma'} |u|_\sigma^2(r) |u|_{\sigma'}^2(r) \epsilon_{R_s}(q_n)$$

$$\times \int \exp[\pm i(\vec{q}_{c_n} - \vec{q}_{c_i}) \cdot \vec{R}_k]$$

$$\times \Theta(r - a) d\vec{R}_k d\vec{q}_{c_i}$$

$$= \pm (2\pi)^2 \sum_{\sigma, \sigma'} |u|_\sigma^2(\vec{r}) |u|_{\sigma'}^2(\vec{r}) \epsilon_{R_s}(q_i)$$

$$\times \Theta(r - a) \Theta(q_{c_n} - q_{c_i}), \quad i \neq k. \tag{2.19}$$

The expression in Eq. (2.19) at $q_{c_n} \equiv 2\pi/R \to 0$, $\vec{R} = \vec{R}_s + \vec{r}$ trends to a pseudopotential at the Dirac point:

$$V_{i, R_s}(\vec{r}) = \pm (2\pi)^2 \epsilon_{R_s}(q_i) \Theta(\lambda_i - R) \Theta(a - r)$$

$$\times \sum_{\sigma, \sigma'} |u|_\sigma^2(r) |u|_{\sigma'}^2(r), \tag{2.20}$$

where $\lambda_i = \frac{2\pi}{q_i}$. This staircaselike (cos-shaped) potential in Eq. (2.20) resembles the experimental one shown in Fig. 1(b). The Hamiltonian with the approximate pseudopotential of staircase type in Eq. (2.20) has a set of quasi-zero-energy levels. This feature of the artificial atom is like a very high principal quantum number for ultraheavy atoms. The values of the radial step V_0 for all these resonances are close; that explains the experimental data in Ref. [7] without invoking speculative assumptions, for example, about the shift of the Dirac touchings in the process of STM probing.
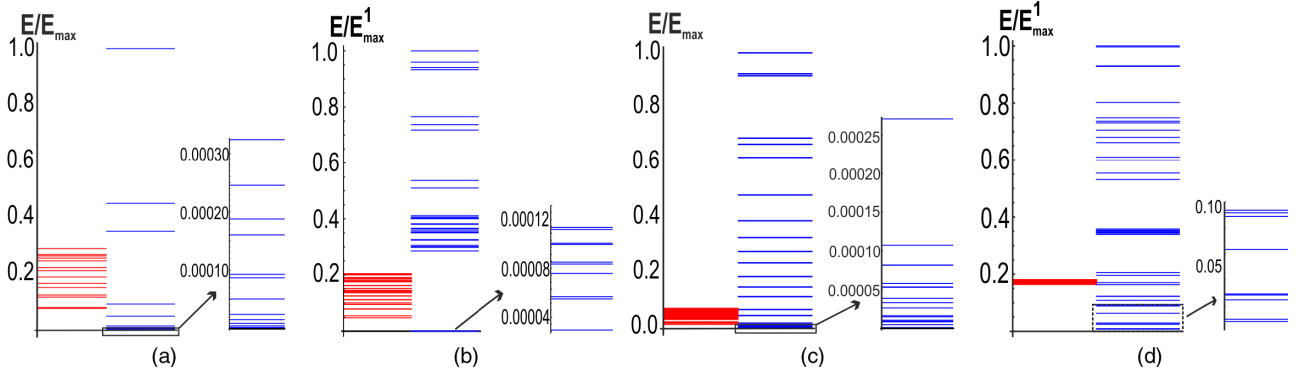
FIG. 3. Energy spectra for graphene quantum dots (GQDs) with topology (a) and (b) $S^1 \times S^1$ and (c) and (d) S^2 on (a) and (c) low-energy and (b) and (d) high-energy scales. In each figure, the left and right spectra correspond to the calculations in the folding zone and pseudopotential approximations, respectively. All spectra are normalized to the largest value of the right spectrum.

Now we solve the following eigenproblem

$$\sum_j \langle \Psi_{c_n} | \hat{H}_D(\vec{R}) | \Psi_{c_j} \rangle \langle \Psi_{c_j} \vec{R}, \sigma \rangle$$

$$+ \sum_m \langle \Psi_{c_n} | V_{\mathrm{GQD}}(\vec{R}) | \Psi_{c_m} \rangle \langle \Psi_{c_m} | \vec{R}, \sigma \rangle$$

$$= E \langle \Psi_{c_n} | \vec{R}, \sigma \rangle. \qquad (2.21)$$

III. RESULTS AND DISCUSSION

A. Emergence of quasi-zero-energy band

To fit a derivative dI/dV of the STM current I with respect to the bias V, it is necessary to calculate LDOS. LDOS reads

$$\rho(\vec{R}, E) = \sum_i \left| \Psi_i(\vec{R}) \right|^2 \delta(E - \epsilon_i), \qquad (3.1)$$

where the summation is performed over all eigenstates of the system. The presence of δ functions reflects the infinitely small spectral line width of an eigenstate. For a finite spectral line width, we have to assign some decay rate γ_i to a given eigenstate and to use the δ function approximation, resulting in a Lorentzian spectral line form

$$\rho(\vec{R}, E) = \sum_i \frac{\left| \Psi_i(\vec{R}) \right|^2}{|E - \epsilon_i + \iota \gamma_i|^2} = \sum_i \frac{\left| \Psi_i(\vec{R}) \right|^2}{(E - \epsilon_i)^2 + \gamma_i^2}. \qquad (3.2)$$

In practice, γ_i are considered as given parameters in a way not to overlap spectrum lines of interest. In our numeric simulation, we have chosen $\gamma = 10^{-3}$ for upper eigenstates and $\gamma = 10^{-5}$ for the lower part of eigenstates. The simulation is time consuming for LDOS. It has been performed at a 32 core cluster with message passing interface parallelization; the simulation time for a single LDOS point is about 10 min.

LDOS determined by the formula in Eq. (3.2) depends on three variables: two space variables and the energy. At least, in modern STM experiments, all directions of charge-current vector for the dot contribute to the tunneling current. Therefore, it is necessary to perform a contour-averaging procedure. We perform averaging over some contour in $\vec{r}$ space accounting for points equivalent from the viewpoint of lattice symmetry. For the toroidal GQD, we choose averaging contours C_T around a center of the 2D toriclike region from three

rhombuses closed sequentially on each other, accounting for graphene lattice symmetry. For the spherical GQD, we choose averaging circles C_S with increasing radii around a point in the center of the rhombus side, accounting for graphene lattice symmetry. The contours C_T and C_S are topologically equivalent to closed contours on the torus and sphere.

We study the LDOS spectra at two relevant competing energy scales. For the torus and sphere topologies, we choose the low- and high-energy ranges 0.24–0.92 eV and 0.68–2.94 eV and, respectively, 0.24–1.22 eV and 2.98–3.26 eV. The scales were obtained in the following way. For the low-energy range, we get the solutions of the conditions of quantization in Eqs. (2.3) and (2.4) for m_1, $m_2 \in [-25, 25]$, which corresponds to the choice of the 40 lowest energy levels from 2601. For the high-energy interval, we determine the solutions of the conditions of quantization in Eqs. (2.3) and (2.4) for m_1, $m_2 \in [-12, 12]$, which corresponds to the choice of the 40 lowest energy levels from 625. Comparing the structures of the levels $E_D(\vec{k}_i)$ and $E^{(0)}(\vec{k}_i)$, $i = 1, \dots, 40$ for the pseudo-Dirac GQD model and our GQD model with Weyl nodes-antinodes, respectively, in the folding zone approximation, we conclude that the Weyl nodes-antinodes decrease the degree p_d of level degeneration. The effects of topology and symmetry manifest themselves in different maximum values of p_d for the sphere and torus topologies in the folding zone approximation. The maximum values $\max(p_d)$ are equal to 4 and 12 for the pseudo-Dirac spherical and toroidal quantum dot models, respectively. In the case of Weyl node-antinode pairs, $\max(p_d)$ takes values of four and six for the spherical and toroidal quantum dot models, respectively. The pseudopotential completely lifts the degeneration of the levels $E^{(0)}(\vec{k}_i)$, $i = 1, \dots, 40$, and the resulting spectrum $E_i^{(1)}$, $i = 1, \dots, 40$ consists of two bands. The lower energy band formed by levels located near the zero-energy $E = 0$ is a quasi-zero-energy band, as one can see in Fig. 3. The spectra for both toroidal and spherical quantum dots in the pseudopotential approximation possess a very narrow quasi-zero-energy band.

B. Toroidal quantum dot

Figure 4 shows the squares $|\Psi_i|^2 = \sum_{j=1}^2 \Psi_{ij}^* \Psi_{ij}$ of the absolute values of ith spinor wave functions. "Hills" in Fig. 4 represent electron states. A bottom view of the 3D plot is

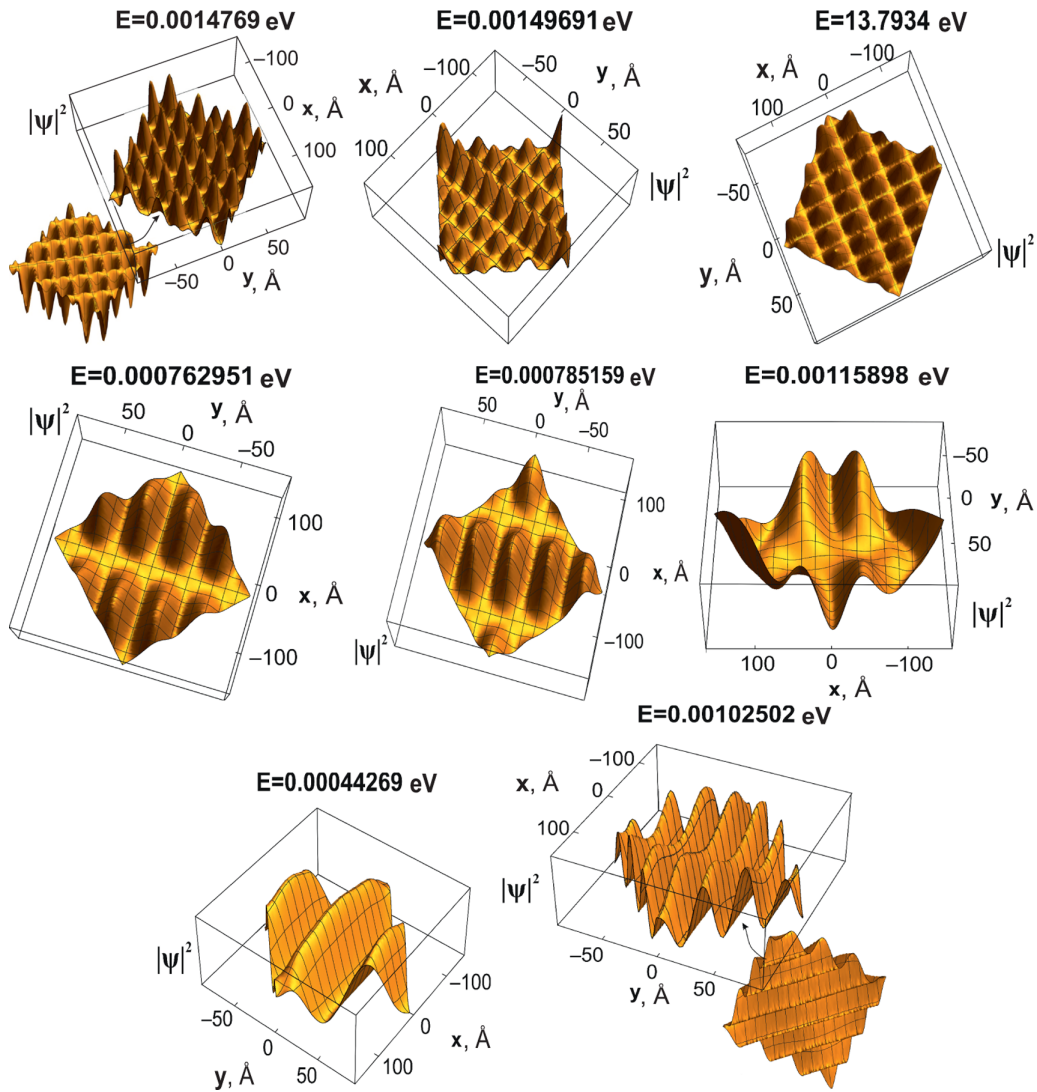FIG. 4. The pseudopotential confinement of the $S^1 \times S^1$-dot states. Squares $|\Psi|^2$ of the absolute values of wave functions are presented. The states are localized on resonant (upper row) and nonresonant (middle row) trajectories of the torus or delocalized due to Klein transitions (bottom row) for the different energies E. For the levels $E = 0.0014769$, 0.00102502 eV, we represent both sightseeing from up and from down.

shown in the inset, upper row, Fig. 4. "Wells" in the inset represent hole states. At definite energies corresponding to resonant trajectories on the torus, the orbitals are like those for Bohr atoms when the length of the closed orbit is an integer number of wavelengths. Due to the zero curvature of the torus, the motion of the charge carrier on such orbits is stable. There also exist other energy levels (Fig. 4, bottom row). On them, the phases of wave functions are multiples of $\pi \pm 2\pi n$, $n = 0, 1, \ldots$. The latter feature makes them like transmission resonances of the Klein tunneling process. Charge carriers delocalized due to the Klein tunneling can be considered, in analogy with atomic states, as valence ones. The localized states are like the core electrons of an atom.

According to Fig. 5, the main feature of the structure of energy levels for the toroidal quantum dot is the presence of self-similar energy bands located subsequently one after another on the energy scale. The atomlike structure (LDOS) for some bands marked by dashed lines in Fig. 5 is realized only for toroidal GQDs, from the geometric viewpoint, due

to the absence of the curvature of a torus. These levels are occupied by electrons (holes) with wave functions of the type of Bohr atom orbital [Fig. 4 (upper row)]. The electron (hole) density can be localized also in the case of nonresonant torus trajectories due to constructive interference [see Fig. 4 (middle row)].

For the toroidal GQD, the charge-carrier density is absent on the quasi-zero-energy band due to destructive interference of the states. The latter fact leads to the formation of a pseudogap between the hole and electron bands, providing the absence of the electron density at the center of the quantum dot, like in the case of an ordinary atom.

C. Spherical-type quantum dot

The probability density of states for the quantum dot with sphere topology is shown in Fig. 6. According to a form of the wave functions, the charge carriers are localized due to constructive interference in the case of nonresonant sphere
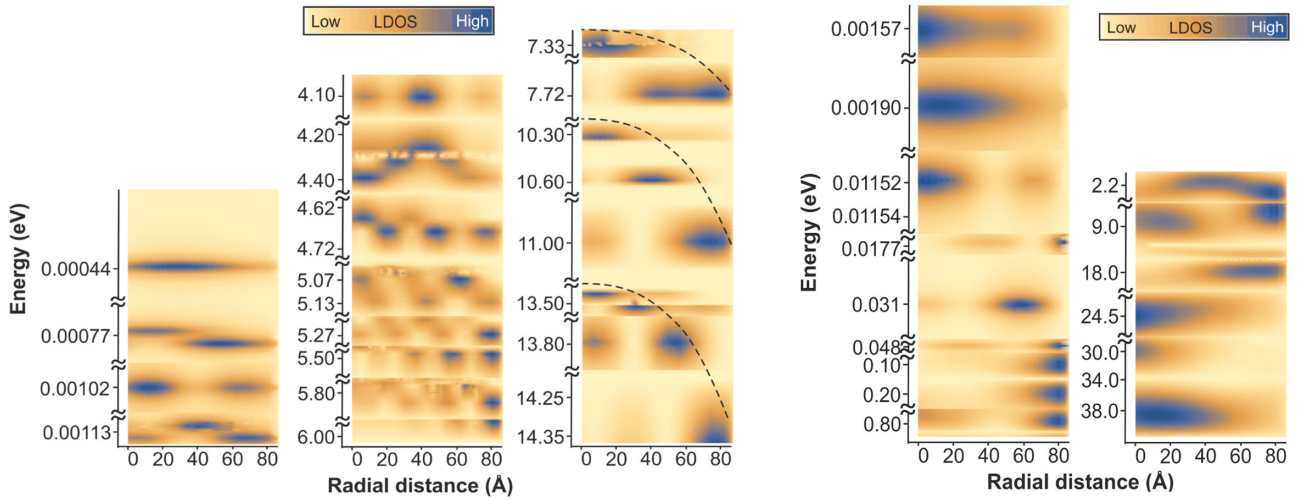
FIG. 5. Local density of states (LDOS) of a toroidal quantum dot in bending bands. (left) LDOS for the states possessing high energies in the folding zone approximation. (right) LDOS for the states possessing low energies in the folding zone approximation. The self-similar bands are marked by dashed lines.

configurations [Fig. 6(a)] or the transmission resonances delocalized in a limited region at the state phase multiple to π [Figs. 6(b)–6(e)]. The resonances of the S^2 dot reside in the quasicirclelike region located either inside one rhombic cell or in two conjugate rhombuses. Therefore, the spherical-type dot can be classified as a quasicircular quantum dot electrostatically confined in one or two supercells bordering on each other. The action of centrifugal forces stipulated by the sphere curvature destroys Bohr atom orbitals formed on resonant trajectories (with an integer number of wave periods on the trajectory). However, such features of the atomic structure as localized "core" charge carriers, and delocalized valence states remain. The "transmission resonances" play a role of the valence states.

Figure 7 demonstrates that the structure of energy levels for the spherical-type GQD hosts self-similar energy bands placed subsequently one after another on the energy scale, and the levels can hold a multiresonance structure. This feature resembles that of the toroidal quantum dot. The electron (hole) density with such a structure is confined by a staircaselike (cos-shaped) potential, as one can see in Figs. 7(b) and 7(c). Opposite to the case of the toroidal quantum dot, the charge-carrier density in the spherical quantum dot resides also on the quasi-zero-energy band [see Fig. 7(a)]. The localized nonresonant electron (hole) configurations shown in the middle row,

Figs. 4 and 6(a), are observed for both spherical and toroidal GQDs.

D. Comparison with experimental data

We now compare the measured experimentally and theoretically predicted distributions of the charge density in electrically confined GQDs.

In Ref. [7], graphene *p-n* junctions with an atomlike structure have been epitaxially grown up to a size of 8 nm along radius R on a copper support. Figures 8(a) and 8(c) show different theoretical predictions for LDOS of the small-radius *p-n* junction, whose spectroscopic map of the radially averaged derivative dI/dV of a STM current I with respect to the bias V is shown in Fig. 8(b). Their features are brought together in Table I. The value of the first level has been chosen as the origin for the energy. We take the graphene dielectric constant $\epsilon = 2.0$. Our estimation of the graphene dielectric constant is consistent with the experimental one equal to 2.2 for graphene carrier concentration $n \sim 10^9$ cm^{-2} [33]. We observe the following differences between the spectroscopic map, LDOS for our toroidal graphene junction model, and LDOS estimated on the assumption that the confining *p-n* junction potential is a radial step. Our level prediction is extremely precise. Their structure and arrangement are also
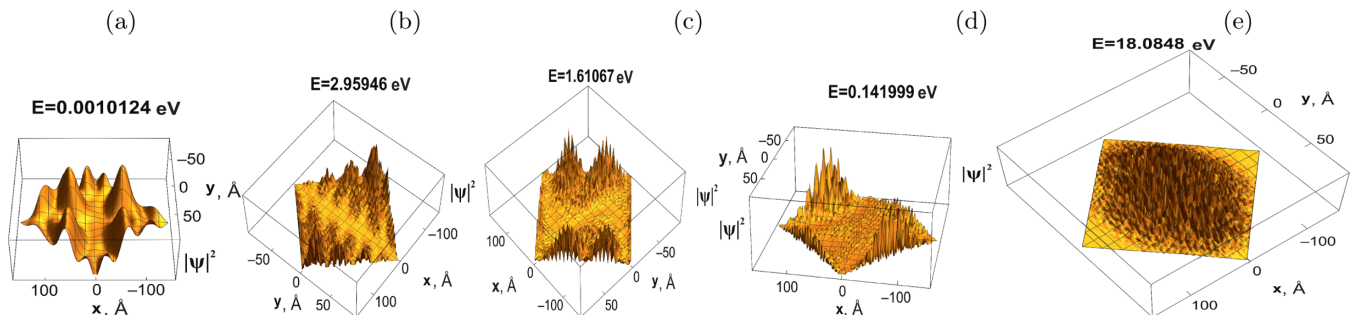

FIG. 6. The pseudopotential confinement of S^2-dot states with different energies E. Squares $|\Psi|^2$ of the absolute values of wave functions are presented. The states are localized on non-resonant trajectories of sphere (a) or are delocalized due to Klein transitions (b–e).
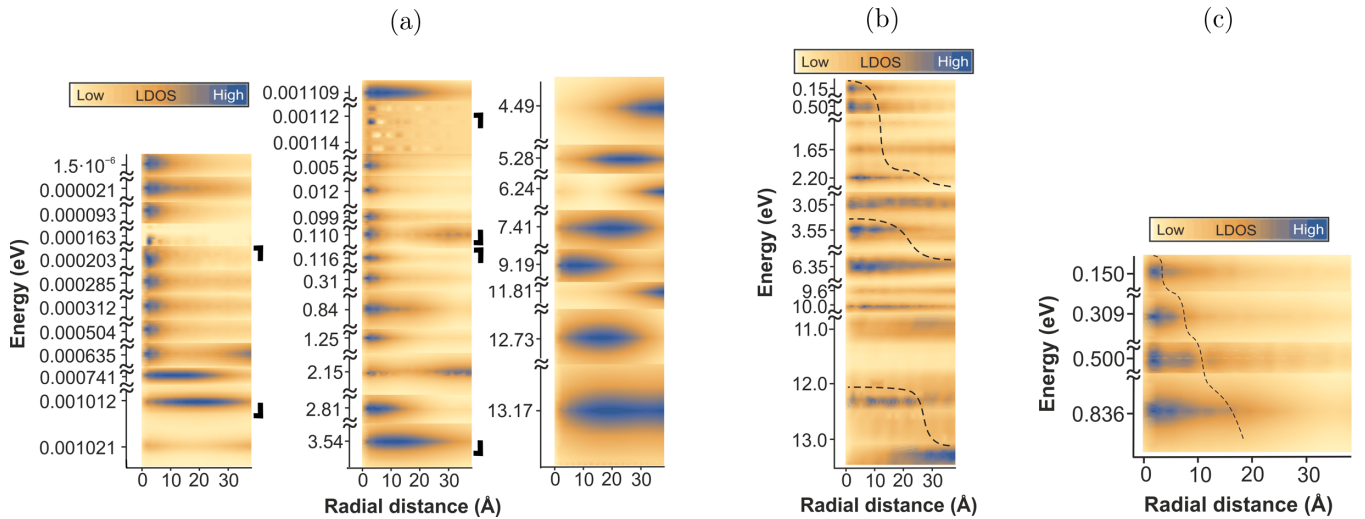
FIG. 7. Local density of states (LDOS) of a spherical quantum dot in bending bands. (a) LDOS for the states possessing low energies in the folding zone approximation. (b) LDOS for the states possessing high energies in the folding zone approximation. (c) A band in the overlapping energy range. Self-similar bands are marked by dashed lines and bold angles.

in perfect agreement with the experimental ones. The second level of our model is unscreened. Higher lying states are screened. The fitting based on the low-energy pseudo-Dirac model Hamiltonian with a radial step potential gives not only values which are very different from the experimental ones but also an incorrect resonance structure because the third level of the junction is doubled. As one can see, a serious drawback of the theoretical approach [7] is also the absolute inability to describe correctly the form of resonances: the theoretically predicted resonances are localized in energy (very narrow) and are spread in space. However, the energy levels of experimental quantum dots are strongly widened in energy and localized in space. The states of the toroidal graphene junction under the action of the pseudopotential are strongly spatially localized and are broadened in energy E (see Fig. 8) as in the experiment. It is easy to see that the experimental confining potential is a parabolic type only. Our numerical results indicate also that a parabolic potential approximates the confining potential.

We conclude that the strength of the electric field created by electrons of the lowest first level is not sufficient for the production of electron-hole pairs. However, the electrical field strength of the electrons of the lowest two first and second levels is strong enough to produce the electron-hole pairs.

Therefore, a screened confining pseudopotential acts on electrons of the third and subsequent levels.

In Ref. [6], a large GQD with a radius of 150 nm was fabricated by the local embedding of a gate in a graphene/h-BN heterostructure on SiO$_2$. Let us compare a theoretical LDOS for the continuous model of a quantum dot with torus topology [Fig. 9(a)] and a second derivative $\frac{d^2I}{dV^2}$ of a STM current I measured as a function of the bias V and the radial distance from the center of the circular graphene p-n junction deposited on BN/SiO$_2$ [Fig. 9(b)]. Our numerical calculation of LDOS predicts the levels with a multiresonance structure. These levels are completely analogous to multiresonance structures of the corresponding experimental levels. An attempt has been made to explain these experimental data using a model of massless pseudo-Dirac fermions in a parabolic potential in Ref. [6]. It turns out that some theoretical levels predicted by this low-energy pseudo-Dirac theory of a large graphene p-n junction are experimentally unobservable. Additionally, some levels experimentally observable are absent in the theory. For example, the pseudo-Dirac model of a circular GQD does not predict the highest experimental energy level of ~80–85 mV (this level is absent). Moreover, all levels with the same numbers of resonances predicted by this pseudo-Dirac fermion model Hamiltonian are arranged in pairs. However,

TABLE I. Assignment of theoretically predicted quantum-dot resonances to experimental data. The resonances are arranged in ascending order of distance from the center of the quantum dot and are measured from the deepest level.

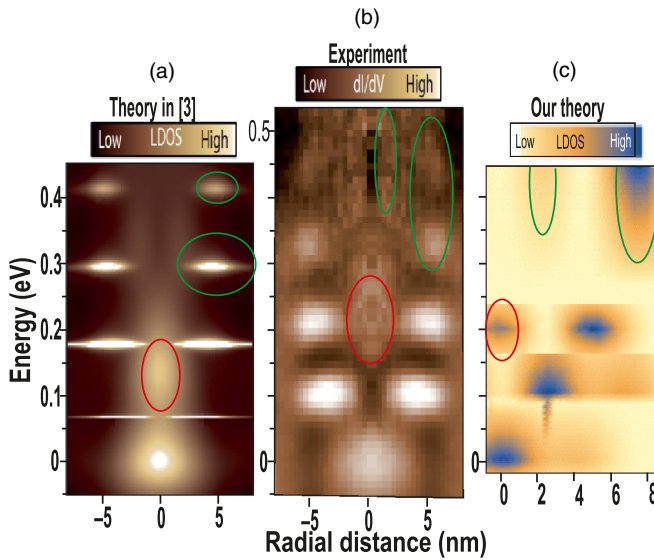| Level number	A number of resonances	Resonance energies, eV		
		Experiment	Our theory	Theory in Refs. [7,34]
First	One	0	0	0
Second	One	0.108	0.109[a]	0.064
Third	Two	0.213	0.194	0.13, 0.175
Fourth	One	0.46	0.51	0.29
Fifth	One	0.42	0.48	0.415

[a]Unscreened level.

FIG. 8. Spectrum of atomlike small graphene quantum dot (GQD). The background correction (chemical potential) μ has been subtracted from the raw data, leading to a shift in the energy so that the energy of lowest resonance in the potential well is zero one. (a) Calculated results presented in Ref. [7] using the radial step potential. (b) The dependence of derivative dI/dV of a scanning tunneling microscope (STM) current I with respect to the bias V as a spectroscopic map of GQD deposited on a copper support [7]. (c) Our results calculated with the graphene dielectric constant $\epsilon = 2$, except the two lowest levels with $\epsilon = 1$; the unscreened band of the continuous toroidal model GQD under the action of a pseudopotential is placed in the range 13.35–14.35 eV.
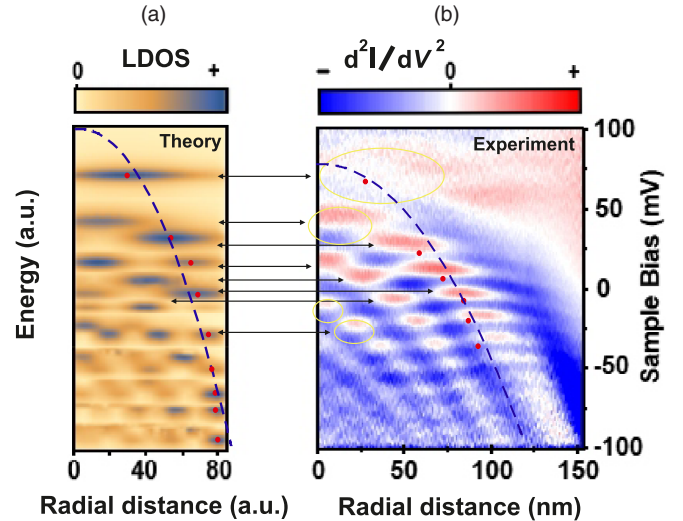

FIG. 9. Energy levels of spatially distributed states of a large graphene quantum dot (GQD). (a) Theoretically simulated local density of states (LDOS) in the bands of states confined by a pseudopotential for the continuous model of quantum dot with torus topology. (b) Second derivative $\frac{d^2I}{dV^2}$ of a scanning tunneling microscope (STM) current I measured as a function of the bias V and the radial distance from the center of a circular graphene *p-n* junction deposited on BN/SiO$_2$. Lines with arrows indicate the theoretical bands coinciding with experimental ones. Some resonances are encircled by a yellow oval to improve perception. A fitting parabolic potential is indicated by a dashed line.

the doubling is not confirmed experimentally [see Figs. 9(a) and 9(b)]. The main drawback of the pseudo-Dirac model is as follows: at a bias from zero and lower, the number of levels in the experiment is twice less than that predicted theoretically.

Finally, let us consider the low-energy region from -50 to -100 mV (corresponding theoretically calculated levels are placed at -50 meV and lower). Contrary to LDOS in the pseudo-Dirac model, the experimental LDOS and the theoretical LDOS confined by the pseudopotential are redistributed to the border of the GQD. Correspondingly, its hole density is polarized.

Let us compare the experimental data on tip-induced electrically confined GQDs in a graphene monolayer covering a 30-nm-thick BN flake on graphite with our numerical calculations of a quantum dot with sphere topology. The sphere has a nonzero curvature leading to a staircaselike (cos-shaped) pseudopotential in Fig. 7(c). This result is in complete agreement with the experimental fitting shown in Fig. 1(b). The pushing out of electrons by the "centrifugal force" onto the quasi-zero-energy band is revealed as the nonzero electron density on its levels.

By compensating the action of a pseudopotential, for example, by the Lorentz force, one can achieve a weak bending of the bands by a pseudopotential with the grouping of nondegenerate levels as in the folding zone approximation. According to our theory of graphene *p-n* (*n-p*) junctions with sphere topology, the multiplicity of energy-level degeneration

p_d in the folding zone approximation is 2, 4, like in the experiment [4]. Moreover, the multiresonance distribution of LDOS over the energy levels for the GQD with sphere topology in Fig. 7 leads to the experimentally observed independence of the charging peak sequence on the distance between the cantilever STM tip and the quantum-dot center. The above discussion allows us to classify this electrostatically confined quantum dot on the BN/graphite support as a spherical one.

Thus, the theoretical predictions of the continuous model of a quantum dot in monolayer graphene with one Dirac point and six pairs of Weyl nodes-antinodes under the action of a pseudopotential not only explain but show the excellent quantitative agreement with various experiments.

IV. CONCLUSIONS

In this paper, we have utilized the rhombic and rectangular graphene supercells to describe the confinement of electrons and holes. Discrete and continuous atomlike models of graphene electrically confined GQDs with the topology of a torus and sphere have been proposed. The charge carriers are confined through polarization effects also. The electron-hole states localized and delocalized in the pseudopotential are calculated in the continuous approximation. The polarization of the GQD due to the pseudopotential "pushes out" the energy levels and lifts their degeneration.

The resonances of the toroidal GQD are partitioned into three types of resonances: strongly and weakly localized

"core electrons" and wave packages for delocalized "valence electrons." We assume that the strong localization may be a consequence of commensurate frequencies of the Hamiltonian system on the torus. The strongly localized states of the toroidal quantum dot are formed as in a Bohr atom. For the toroidal quantum dot, the electron (hole) density is absent on the quasi-zero-energy band due to the zero curvature of the torus. This leads to the formation of a pseudogap between the hole and electron bands, which ensures the absence of the charge density at the center of the quantum dot, like at the center of the Bohr atom. Accordingly, the toroidal-type quantum dot is an artificial atom with Bohr orbits.

Unlike the toroidal quantum dot, the spherical GQD hosts multiresonances, whose charge density is present at its quasi-zero-energy band. Accordingly, three spherical dots of the hexagonal quantum dot can play a role of the nucleus of the artificial atom.

To summarize, the quasirelativistic model graphene *n-p* (*p-n*) junctions with the supercell pseudopotential which electrically confines electrons (holes) have been proposed. This potential can bend energy levels in a parabolic way. For GQDs with the sphere topology, the parabolic potential is additionally modulated staircase (cos-shaped) wise. This approach explains the main features of local distribution of charge-carrier density for the quantum dots observed in various STM experiments. The advantage of the approach we develop is the ability not only to correctly predict the arrangement of levels but also to describe the phenomenon of polarization in GQDs.

[1] J. Zhang and S.-H. Yu, Mater. Today **19**, 382 (2016).
[2] N. N. Bogolubov, A. V. Soldatov, and S. P. Kruchinin, Quantum Matter **4**, 352 (2015).
[3] V. V. Kudryashov, Nonlinear Phenom. Complex Syst. **12**, 199 (2009).
[4] N. M. Freitag, L. A. Chizhova, P. Nemes-Incze, C. R. Woods, R. V. Gorbachev, Y. Cao, A. K. Geim, K. S. Novoselov, J. Burgdörfer, F. Libisch, and M. Morgenstern, Nano Lett. **16**, 5798 (2016).
[5] Y. Jiang, J. Mao, D. Moldovan, M. R. Masir, Gu. Li, K. Watanabe, T. Taniguchi, F. M. Peeters, and E. Y. Andrei, Nat. Nanotechnol. **12**, 1045 (2017); J. Mao, Y. Jiang, D. Moldovan, G. Li, K. Watanabe, T. Taniguchi, M. R. Masir, F. M. Peeters, and E. Y. Andrei, Nat. Phys. **12**, 545 (2016).
[6] J. Lee, D. Wong, J. Velasco Jr., J. F. Rodriguez-Nieva, S. Kahn, H.-Z. Tsai, T. Taniguchi, K. Watanabe, A. Zettl, F. Wang, L. S. Levitov, and M. F. Crommie, Nat. Phys. **12**, 1032 (2016).
[7] C. Gutiérrez, L. Brown, C.-J. Kim, Jiwoong Park, and A. N. Pasupathy, Nat. Phys. **12**, 1069 (2016).
[8] Yu. Zhao, J. Wyrick, F. D. Natterer, J. R. Nieva, C. Lewandowski, K. Watanabe, T. Taniguchi, L. Levitov, N. B. Zhitenev, and J. A. Stroscio, Science **348**, 672 (2015).
[9] G. Giavaras and F. Nori, Phys. Rev. B **85**, 165446 (2012).
[10] P. A. Maksym, M. Roy, M. F. Craciun, S. Russo, M. Yamamoto, S. Tarucha, and H. Aoki, J. Phys. Conf. Ser. **245**, 012030 (2010).
[11] A. Hansen and F. Ravndal, Phys. Scr. **23**, 1036 (1981).
[12] A. H. Castro Neto, F. Guinea, N. M. R. Peres, K. S. Novoselov, and A. K. Geim, Rev. Mod. Phys. **81**, 109 (2009).
[13] A. Calogeracos, N. Dombey, and K. Imagawa, Phys. Atom. Nucl. **59**, 1275 (1996).
[14] P. Hewageegana and V. Apalkov, Phys. Rev. B **77**, 245426 (2008).
[15] A. Matulis and F. M. Peeters, Phys. Rev. B **77**, 115423 (2008).
[16] T. D. Linh Dinh *et al.*, J. Phys.: Condens. Matter **30**, 315501 (2018).
[17] K. Nakada, M. Fujita, G. Dresselhaus, and M. S. Dresselhaus, Phys. Rev. B **54**, 17954 (1996); H. P. Heiskanen, M. Manninen,

and J. Akola, New J. Phys. **10**, 103015 (2008); A. V. Rozhkov, G. Giavaras, Y. P. Bliokh, V. Freilikher, and F. Nori, Phys. Rep. **503**, 77 (2011).
[18] M. Grujic, M. Zarenia, A. Chaves, M. Tadic, G. A. Farias, and F. M. Peeters, Phys. Rev. B **84**, 205441 (2011).
[19] Z. Z. Zhang, K. Chang, and F. M. Peeters, Phys. Rev. B **77**, 235411 (2008).
[20] P. Potasz, A. D. Güçlü, and P. Hawrylak, Phys. Rev. B **81**, 033403 (2010).
[21] K. A. Ritter and J. W. Lyding, Nat. Mater. **8**, 235 (2009).
[22] G. Pal, W. Apel, and L. Schweitzer, Phys. Rev. B **84**, 075446 (2011).
[23] J.-R. Wang and G.-Z. Liu, J. Phys.: Condens. Matter **23**, 155602 (2011).
[24] L. L. Li, M. Zarenia, W. Xu, H. M. Dong, and F. M. Peeters, Phys. Rev. B **95**, 045409 (2017).
[25] S. Reich, C. Thomsen, and J. Maultzsch, Carbon nanotubes, in *Basic Concepts and Physical Properties* (Wiley-VCH Verlag GmbH & Co. KGaA, Wenheim, 2004).
[26] H. V. Grushevskaya and G. Krylov, J. Mod. Phys. **5**, 984 (2014).
[27] H. V. Grushevskaya and G. Krylov, Nonlinear Phenom. Complex Syst. **18**, 266 (2015).
[28] H.-Zh. Lu and Sh.-Q. Shen, Front. Phys. **12**, 127201 (2017).
[29] J. C. Phillips and L. Kleinman, Phys. Rev. **116**, 287 (1959).
[30] V. A. Fock, *Fundamentals of Quantum Mechanics* (Mir Publishing, Moscow, 1978).
[31] H. Krylova and L. Hurski, *Spin Polarization in Strongly Correlated Systems* (LAP Lambert Academic Publishing, Saarbrücken, 2013).
[32] A. Altland and B. Simons, *Condensed Matter Field Theory* (Cambridge University Press, New York, 2010).
[33] D. C. Elias, R. V. Gorbachev, A. S. Mayorov, S. V. Morozov, A. A. Zhukov, P. Blake, L. A. Ponomarenko, I. V. Grigorieva, K. S. Novoselov, F. Guinea, and A. K. Geim, Nat. Phys. **8**, 172 (2012).
[34] H. Ch. Nguyen, N. T. T. Nguyen, and V. L. Nguyen, J. Phys.: Condens. Matter **29**, 405301 (2017).